Available online at www.sciencedirect.com

ScienceDirect

Geochimica et Cosmochimica Acta 155 (2015) 154–171

Geochimica et Cosmochimica Acta

www.elsevier.com/locate/gca

Paleotemperatures at the lunar surfaces from open system behavior of cosmogenic ^{38}Ar and radiogenic ^{40}Ar

David L. Shuster[a,b,*], William S. Cassata[c]

[a] Department of Earth and Planetary Science, University of California, Berkeley, CA 94720-4767, USA
[b] Berkeley Geochronology Center, 2455 Ridge Road, Berkeley, CA 94709, USA
[c] Chemical Sciences Division, Lawrence Livermore National Laboratory, 7000 East Avenue (L-231), Livermore, CA 94550, USA

Received 30 July 2014; accepted in revised form 31 January 2015; Available online 11 February 2015

Abstract

The simultaneous diffusion of both cosmogenic ^{38}Ar and radiogenic ^{40}Ar from solid phases is controlled by the thermal conditions of rocks while residing near planetary surfaces. Combined observations of ^{38}Ar/^{37}Ar and ^{40}Ar/^{39}Ar ratios during stepwise degassing analyses of neutron-irradiated Apollo samples can distinguish between diffusive loss of Ar due to solar heating of the rocks and that associated with elevated temperatures during or following impact events; the data provide quantitative constraints on the durations and temperatures of each process. From sequentially degassed ^{38}Ar/^{37}Ar ratios can be calculated a spectrum of apparent ^{38}Ar exposure ages versus the cumulative release fraction of ^{37}Ar, which is particularly sensitive to conditions at the lunar surface typically over $\sim 10^6$–10^8 year timescales. Due to variable proportions of K- and Ca-bearing glass, plagioclase and pyroxene, with variability in the grain sizes of these phases, each sample will have distinct sensitivity to, and therefore different resolving power on, past near-surface thermal conditions. We present the underlying assumptions, and the analytical and numerical methods used to quantify the Ar diffusion kinetics in multi-phase whole-rock analyses that provide these constraints.

For Apollo 15 samples 15016, 15556, and 15596 we find apparent ^{40}Ar/^{39}Ar plateau ages between 3.21 and 3.28 Ga and evidence for diffusive loss of radiogenic ^{40}Ar primarily from K-bearing glass. From ^{38}Ar/^{37}Ar spectra normalized to the apparent Ca/K ratios, we also find evidence of diffusive loss of cosmogenic ^{38}Ar that requires elevated temperatures either during or after surface exposure. Using ^{39}Ar and ^{37}Ar, we construct multiple-phase–multiple diffusion domain (MP-MDD) models to quantify the diffusion kinetics of Ar from a range of macroscopic grain sizes of each phase. While diffusive loss of ^{40}Ar can be explained by brief reheating conditions after crystallization (e.g., during an impact event), we find that both the radiogenic ^{40}Ar and cosmogenic ^{38}Ar abundances can be explained by internally consistent thermal conditions expected for solar heating of the rocks at the lunar surface. These conditions correspond to effective diffusion temperatures (*EDT*, i.e., the temperature corresponding to the mean diffusivity over temperature variability) between 65 and 81 °C, with an error-weighted mean of 77.0 ± 1.3 °C, despite differences in diffusion kinetics and large differences in surface exposure duration between the three samples (~56–621 Ma). This *EDT* corresponds to a maximum daytime temperature of ~96 °C, which is in excellent agreement direct measurements of temperature at the Apollo 15 landing site. The open system behavior in both a radiogenic and a cosmogenic nuclide provides tests for internal consistency in best-fitting solutions of time-integrated thermal conditions of rocks collected from planetary surfaces. This thermal information is important for the study of habitable conditions at planetary surfaces, and has implications for Ar-based geochronology and paleomagnetic observations applied to planetary materials.

---

* Corresponding author at: Department of Earth and Planetary Science, University of California, Berkeley, CA 94720-4767, USA. Tel.: +1 510 642 2607.

E-mail address: dshuster@berkeley.edu (D.L. Shuster).

http://dx.doi.org/10.1016/j.gca.2015.01.037
0016-7037/

1. INTRODUCTION

^{40}Ar/^{39}Ar thermochronometry is broadly used to interpret geochemical, chronologic, and petrologic data acquired from rocks and minerals, and to study a variety of planetary processes (e.g., exhumation, metamorphism, shock heating, etc.). In many instances, the geologic context of a sample informs the construction of plausible thermal and dynamic models. For example, to interpret ^{40}Ar/^{39}Ar data obtained from an exhumed Himalayan K-feldspar of plutonic origin, Richter et al. (1991) modeled the conductive cooling of an un-roofing pluton. In other instances, the appropriate thermal model to consider may be unclear. This is especially true for lunar and meteorite samples, where contextual associations are generally lacking. In these instances, ^{40}Ar/^{39}Ar age spectra alone may not be sufficient to constrain a sample's thermal history.

Our recent efforts to determine the thermal histories, and thus constrain the age of paleomagnetic properties, of several lunar rocks highlight the significance of this problem (Shea et al., 2012; Suavet et al., 2013; Tikoo et al., 2014). Lunar mare basalts from the Apollo 12, 14, and 15 sites retain primary natural remnant magnetization (NRM) consistent with cooling in the presence of a relatively strong magnetic field. It was unclear whether this magnetic field was transient (i.e., generated by an impact event) or long-lived (i.e., generated by a core dynamo). While the former scenario implies NRM acquisition during short-lived thermal events associated with impacts, the latter implies NRM acquisition during primary igneous cooling. Our objective was thus to determine if discordance observed on the mare basalt age spectra was due to high temperature heating in excess of the Curie point (i.e., during an impact event; Cassata et al., 2010; Shuster et al., 2010) or low temperature heating associated with solar heating at the lunar surface (e.g., Turner, 1971). However, without geologic context, the ^{40}Ar/^{39}Ar age spectra alone cannot always discriminate between these scenarios.

It is also possible to construct an exposure age spectrum based on the release of cosmogenic ^{38}Ar (^{38}Ar$_{\text{cos}}$) relative to calcium-derived ^{37}Ar (^{37}Ar$_{\text{Ca}}$) and potassium-derived ^{39}Ar (^{39}Ar$_{\text{K}}$), as Ca and K are the principle spallation target elements in samples analyzed for ^{40}Ar/^{39}Ar thermochronometry (e.g., Turner et al., 1971). The exposure age spectrum is directly analogous to the radioisotopic age spectrum based on the release radiogenic ^{40}Ar relative to ^{39}Ar$_{\text{K}}$, but with the added complexity of production from K and Ca. However, discordance in the cosmogenic exposure age spectrum provides a means to assess diffusive loss of Ar associated with solar heating or small impacts at the lunar surface, irrespective of prior thermal events. Employing this approach, we found that discordance in cosmogenic ^{38}Ar exposure age spectra observed on the mare basalt age spectra could be explained entirely by diffusive loss at near surface temperatures, and thus no high temperature heating was required to explain the ^{40}Ar/^{39}Ar age spectra (Shea et al., 2012; Suavet et al., 2013; Tikoo et al., 2014).

Combined modeling of radioisotopic and exposure age spectra provides a method to study lunar and meteorite samples, where complex, multistage thermal histories are anticipated. Such detailed thermal constraints have potential to improve our understanding of both discordant radioisotopic ages (e.g., differences between Rb–Sr, K–Ar, and Sm–Nd ages) and cosmogenic exposure ages (e.g., differences between ^{38}Ar, ^{21}Ne, and ^{3}He ages). Moreover, the exposure age spectrum provides an internal assessment of accuracy in that a "plateau" segment should exist for samples that have not been extensively heated after cosmic ray exposure began. Collectively, improved accuracy in cosmogenic nuclide dating and a better understanding of open system behavior of cosmogenic noble gases should permit more robust empirical determinations of cosmogenic nuclide production rates.

In this paper, we detail our method for constraining the thermal conditions of rocks exposed at the lunar surface based on open-system behavior of both cosmogenic ^{38}Ar and radiogenic ^{40}Ar. We discuss the underlying assumptions of the approach, and the analytical and numerical methods used to determine Ar diffusion kinetics in multi-phase whole-rock analyses, based on ^{37}Ar and ^{39}Ar release, and to quantify thermal histories based on ^{38}Ar and ^{40}Ar release. In section 3, we present new Ar isotopic analyses of Apollo samples 15016, 15556, and 15596 and use these data to quantify diffusion parameters for ^{37}Ar and ^{39}Ar to model the diffusive behavior of cosmogenic ^{38}Ar (^{38}Ar$_{\text{cos}}$) and radiogenic ^{40}Ar (^{40}Ar*) at the lunar surface. Our analysis constrains thermal conditions of solar insolation and impact heating on the moon. As with other mare basalts that we have analyzed, we find that discordance observed on the radioisotopic and exposure age spectra can be explained entirely by daytime heating at the lunar surface. In each instance, diffusive loss from the basalts is principally associated with mesostasis glass. It thus appears that glass fragments are particularly susceptible to Ar loss during near surface residence, consistent with predictions based on laboratory-derived diffusion kinetics (e.g., Hazelton et al., 2003; Gombosi et al., 2015). We discuss the implications of this finding for the accuracy of total fusion analyses of lunar impact spherules and incremental heating analyses of lunar impact melts.

2. SAMPLES AND METHODS

2.1. Apollo samples 15016, 15556, and 15596

The three Apollo samples used in this study were collected within ~2.5 km of one another at the Apollo 15 landing site (Meyer, 2005). Tikoo et al. (2012) reported the paleomagnetic properties of two samples presented here (15016 and 15556). Sample 15016 is a medium-grained, olivine basalt composed of plagioclase (21–27% by volume), pyroxene (59–63%), and olivine (6–10%), with both low-K and high-K glass in the mesostasis (Brown et al., 1972; Papike et al., 1976; McGee et al., 1977); this sample was collected at Station 3. Sample 15556 is a vesicular mare basalt that was collected at Station 9A, ~60 m from the edge of Hadley Rille in a location of thin regolith with abundant rock samples exposed. The rock is fine grained, composed of plagioclase (30–38% by volume), pyroxene (50–57%), and olivine (0.1–5%), with glass in the mesostasis (Butler, 1971; Rhodes and Hubbard, 1973; Meyer, 2005). Sample 15596 is a vuggy vitrophyric pigeonite basalt (Ryder and Spudis, 1987), also collected from Station 9A. This sample was chipped from a small boulder near the edge of Hadley Rille from a location of thin regolith, with abundant rock samples exposed (Meyer, 2005). The boulder was thought to be recent outcrop of bedrock from the side of the rille. The rock is fine grained, composed of plagioclase (~35% by volume), pyroxene (41–65%), and olivine (3–5%), with groundmass that is slightly crystalline (Butler, 1971; Brown et al., 1972; Grove and Walker, 1977). Average chemical compositions of plagioclase, K-bearing glass, and pyroxene obtained by Electron Probe Micro-Analysis (EPMA) are given for each sample in the Supplementary Data (Table S2). Mesostasis glass does not appear to be devitrified in any sample in the thin sections we studied.

2.2. Analytical methods – Ar analyses

Whole rock chips of each sample (with masses of ~5 mg) were sequentially degassed to conduct ^{40}Ar/^{39}Ar and ^{38}Ar/^{37}Ar thermochronometry at the Berkeley Geochronology Center following procedures described in Cassata et al. (2009), Shuster et al. (2010), Shea et al. (2012). The samples were loaded into aluminum discs alongside Hb3gr neutron fluence monitors and were irradiated for 100 h at the Oregon State University TRIGA reactor in the Cadmium-Lined In-Core Irradiation Tube (CLICIT) facility. After irradiation, smaller chip aliquots of the irradiated samples were placed within small metal tubes of high purity Pt–Ir alloy and incrementally degassed using feedback-controlled laser heating with a 30 W diode laser (wavelength of 810 ± 10 nm) equipped with a coaxially aligned optical pyrometer. The single-color pyrometer was calibrated against a type-K thermocouple under high vacuum (<10^{-8} torr) and under the same conditions as the degassing analyses to correct for the temperature dependent emissivity of the Pt–Ir tubes. Since the objective of this study is to interrogate the natural spatial distributions of radiogenic ^{40}Ar and cosmogenic ^{38}Ar in multiple phases, it is important that the geometries of the diffusion domains (i.e., grain boundaries) remained intact during the analyses. For this reason, we analyzed Ar extracted from whole rock chips, rather than separated minerals or glass, which are often modified during physical disaggregation.

During sequential degassing, the samples were first held under static vacuum at a controlled temperature to within ±10 °C for 600 s (Table S1). The extracted Ar was then purified using one hot and one cold SAES® GP-50 getter pump fitted with C-50 cartridge (St101 alloy). Five isotopes of Ar (^{36}Ar, ^{37}Ar, ^{38}Ar, ^{39}Ar, and ^{40}Ar) were analyzed with a Mass Analyzer Products 215c mass spectrometer using a single Balzers SEV-217 discrete dynode electron multiplier. Corrections for interfering nuclear reaction products (Renne et al., 2005), ^{37}Ar and ^{39}Ar decay, spectrometer discrimination, and extraction line blanks were applied to the measured signals. Apparent ^{40}Ar/^{39}Ar ages were calculated relative to the Hb3gr standard (1081 Ma) using the decay constants and standard calibration of Renne et al. (2011), and isotope abundances of Steiger and Jäger (1977) (full datasets, isotopic corrections, and neutron irradiation parameters appear in Table S1); corrections for trapped and cosmogenic ^{40}Ar were not applied.

2.3. Calculating an apparent ^{38}Ar age spectrum

The apparent cosmic ray exposure ages of each degassing step can be calculated from the ratio of cosmogenic ^{38}Ar (^{38}Ar$_{\text{cos}}$) to reactor-produced ^{37}Ar (^{37}Ar$_{\text{Ca}}$) and ^{39}Ar (^{39}Ar$_{\text{K}}$) according to the following equation:

$$\text{Exposure age} = \left(\frac{^{38}\text{Ar}_{\text{cos}}}{^{37}\text{Ar}_{\text{Ca}}}\right)\left(\frac{\gamma}{\frac{P_{38}}{[\text{Ca}]}}\right) \tag{1}$$

where P_{38}/[Ca] is the production rate of ^{38}Ar$_{\text{cos}}$ relative to the Ca concentration (Turner et al., 1971) and γ is the irradiation parameter relating ^{37}Ar$_{\text{Ca}}$ to Ca content (Levine et al., 2007). Assuming there are only two components of ^{38}Ar and ^{36}Ar, the ^{38}Ar/^{36}Ar ratio quantifies the proportion of cosmogenic and trapped Ar isotopes by mass balance, according to the following equation:

$$^{36}\text{Ar}_{\text{cos}} = {}^{36}\text{Ar}_{\text{T}}\left[1 - \frac{1.54 - (^{38}\text{Ar}/^{36}\text{Ar})_{\text{meas}}}{1.54 - 0.19}\right] \tag{2}$$

where 1.54 is the cosmogenic ^{38}Ar/^{36}Ar ratio (Wieler, 2002) and 0.19 is the trapped ^{38}Ar/^{36}Ar ratio (Levine et al., 2007). P_{38}/[Ca] of each step was calculated using the ^{38}Ar production rate from Ca of Turner et al. (1971) and relative production rates from K, Fe, and Ti of Eugster and Michel (1995)), given by

$$\begin{aligned}\frac{P_{38}}{[\text{Ca}]}\left(\frac{10^{-13}\ \text{moles}\ ^{38}\text{Ar}}{g - \text{Ca}\cdot\text{Ma}}\right) = {} & 6.25 + 10.0\left[\frac{39.1}{40.1}\left(\frac{\text{K}}{\text{Ca}}\right)_{\text{meas}}\right] \\ & + 0.34\left[f_{37_{\text{plag}}}\left(\frac{[\text{Fe}]}{[\text{Ca}]}\right)_{\text{plag}}\right. \\ & \left. + \left(1 - f_{37_{\text{plag}}}\right)\left(\frac{[\text{Fe}]}{[\text{Ca}]}\right)_{\text{glass}}\right] \\ & + 1.31\left[f_{37_{\text{plag}}}\left(\frac{[\text{Ti}]}{[\text{Ca}]}\right)_{\text{plag}}\right. \\ & \left. + \left(1 - f_{37_{\text{plag}}}\right)\left(\frac{[\text{Ti}]}{[\text{Ca}]}\right)_{\text{glass}}\right], \end{aligned} \tag{3}$$

where (K/Ca)$_{\text{meas}}$ is the measured (^{39}Ar$_{\text{K}}$/^{37}Ar$_{\text{Ca}}$) ratio of each step multiplied by a reactor constant (equal to 0.51 for the Oregon State University TRIGA reactor CLICIT position) that relates the production cross sections of ^{39}Ar from K and ^{37}Ar from Ca, elemental concentrations (e.g., [Ca]) are in wt.% and are determined by EPMA (Table S2), and the fraction of ^{37}Ar$_{\text{Ca}}$ derived from plagioclase is given by

$$f_{37_{\text{plag}}} = 1 - \left[\frac{\left(\frac{[\text{K}]}{[\text{Ca}]}\right)_{\text{plag}} - \frac{39.1}{40.1}\left(\frac{\text{K}}{\text{Ca}}\right)_{\text{meas}}}{\left(\frac{[\text{K}]}{[\text{Ca}]}\right)_{\text{plag}} - \left(\frac{[\text{K}]}{[\text{Ca}]}\right)_{\text{glass}}}\right], \tag{4}$$

where the concentration ratio of Ca:K in plagioclase and K-glass is determined by EPMA or a model fit to the incremental release of ^{37}Ar and ^{39}Ar (Table 1). The latter method was employed here, as uncertainties on K concentrations in plagioclase determined by EPMA are

Table 1
Summary of MP-MDD model parameters.

Phase	E_a (kJ/mol)	$\ln(D_o/a^2)_1$	Φ_{1-39}	Φ_{1-37}	Ca/K	P_{38}/[Ca] (mol/g_{Ca}/Ma)	$\ln(D_o/a^2)_2$	Φ_{2-39}	Φ_{2-37}	Ca/K	P_{38}/[Ca] (mol/g_{Ca}/Ma)
15016											
Plagioclase	190	10.5	0.350	0.997	274	4.90×10^{-13}	–	–	–	–	–
K-Glass	143	9.5	0.350	0.001	0.27	3.45×10^{-12}	5.5	0.300	0.002	0.65	1.78×10^{-12}
15556											
Plagioclase	190	10.0	0.400	0.997	241	4.90×10^{-13}	–	–	–	–	–
K-Glass	143	10.0	0.250	0.001	0.39	2.60×10^{-12}	5.5	0.350	0.002	0.55	1.98×10^{-12}
15596											
Plagioclase	178	9.0	0.400	0.997	120	5.07×10^{-13}	–	–	–	–	–
K-Glass	143	11.0	0.200	0.001	0.24	3.84×10^{-12}	5.5	0.400	0	0.24	3.84×10^{-12}

The glass is fit with a two domain model; the plagioclase is fit with an one domain model.

The magnitude of D_o/a^2 is calculated with D in cm^2/s and a in cm.

Φ is the fraction of $^{39}Ar_K$ or $^{37}Ar_{Ca}$ contained within a given domain and is calculated based on the total released in the first 21 or 22 extractions.

P_{38}/[Ca] is the domain-specific production rate for $^{38}Ar_{cos}$ and is calculated based on the relative concentrations of K, Ca, Fe and Ti in plagioclase and K-glass, following Turner et al. (1997).

exceedingly large (see Table S2). Reasonably accurate results would be obtained if no EPMA data were obtained and production from Fe and Ti were not included; production from Ni, Cr, and Mn was ignored. By using this production rate, we assume the samples were exposed directly at the lunar surface, which is a simplification. Since the sample depth beneath the surface likely changed through time due to regolith "gardening" during the exposure duration (e.g., Gault et al., 1974) the apparent exposure ages represent lower bounds on the total durations of residence within several meters of the surface.

A strength of this approach is that exposure age spectra generated from multi-phase samples compensate for Ca and K variations, the dominant sources of cosmogenic ^{38}Ar in most minerals targeted for ^{40}Ar/^{39}Ar chronology, requiring fewer assumptions than employed in previous attempts to generate exposure age plateaus from incremental heating data. For example Turner et al. (1997) plotted the step-wise release $^{38}Ar_{cos}/^{37}Ar_{Ca}$ from a whole-rock analysis of Martian meteorite ALH 84001. A relatively consistent ratio (i.e., a plateau) was obtained at intermediate heating steps. An exposure age was calculated from this plateau segment based on the independently determined chemical composition of the feldspathic glass. Likewise Korochantseva et al. (2007) plotted step-wise exposure ages obtained from plagioclase and pyroxene mineral separates from two desert meteorites. The individual step exposure ages were calculated based on the measured $^{38}Ar_{cos}/^{37}Ar_{Ca}$ ratios and assumed constant mineral-specific production rates, defined by independently determined chemical compositions. While these approaches may yield accurate results, in most samples analyzed for ^{40}Ar/^{39}Ar thermochronometry, Ca and K are the dominant target elements for spallation reactions, and reasonably accurate (within ~5%) exposure age spectra can be generated without external measures of mineral chemistry. In this way, intra-sample variations in production rates (that are characteristic of multi-phase whole-rock samples and zoned minerals) are not manifest in exposure age spectra as discordant steps. However, if a particular phase is rich in Fe, Ti, Mn, Cr, or Ni (e.g., pyroxene), then corrections must be applied to an apparent exposure age that is based solely on ^{38}Ar production from Ca and K.

2.4. Quantifying Ar diffusion kinetics of multiple phases (MP)

During stepwise degassing of whole-rock aliquots, the observed Ar at each step is potentially derived from multiple phases with different diffusion kinetics. In the mare basalts, these phases primarily include potassium-rich aluminosilicate glass (K-glass), plagioclase, and pyroxene. The petrology of these samples (Section 2.1) helps constrain the relative contributions of each phase to the total abundances of observed radiogenic ^{40}Ar ($^{40}Ar^*$), $^{39}Ar_K$, $^{38}Ar_{cos}$, $^{37}Ar_{Ca}$, and $^{36}Ar_{cos}$. K-glass is the primary host of $^{40}Ar^*$ and $^{39}Ar_K$, followed by plagioclase. Plagioclase is the primary host of $^{38}Ar_{cos}$, $^{36}Ar_{cos}$, and $^{37}Ar_{Ca}$, followed by pyroxenes. Our objective is to quantify the kinetics of Ar diffusion in each of these phases. In Section 3 we apply these diffusion parameters to quantify diffusive loss of cosmogenic ^{38}Ar and radiogenic ^{40}Ar.

2.4.1. Quantifying diffusion coefficients

Because both ^{37}Ar and ^{39}Ar are produced solely during neutron irradiation, we assume they are produced with a spatially uniform distribution within solid phases that contain Ca and K. Under this assumption, from the fraction of gas extracted and the duration of each heating step, we calculate a diffusion coefficient normalized to the square of a diffusion length (D/a^2), which we assume to be the radius of a spherical diffusion domain (Fechtig and Kalbitzer, 1966). Although a small proportion of each nuclide will be emitted from the edges of each phase during production due to the range of neutron-generated ^{39}Ar and ^{37}Ar and in solid matter [~0.1 microns (Turner and Cadogan, 1974; Villa, 1997; Jourdan et al., 2007) and ~1.3–1.8 microns (Jourdan and Renne, 2009), respectively], we assume that this effect has a negligible influence on the calculation of diffusion coefficients. We plot the calculated D/a^2 coefficients on an Arrhenius plot [i.e., $\ln(D/a^2)$ versus $1/T$] using the controlled temperature of each extraction. Since multiple phases in these samples contain both K and Ca (Section 2.1), we anticipate that the calculated coefficients will not necessarily define a single linear relationship, yet will reflect the simultaneous diffusion from multiple phases and diffusion domain sizes, which we assume are defined by macroscopic grain dimensions.

2.4.2. MP-MDD model construction and free parameters

Since Ca and K are primarily contained within potassium-rich aluminosilicate glass (K-glass), plagioclase and pyroxene in these samples, we assume these are the only phases that contain ^{37}Ar and ^{39}Ar. As our goal is to use observations of diffusive loss of ^{38}Ar$_{cos}$ and ^{40}Ar* to constrain the low temperature (i.e., near surface) conditions experienced by each sample, we further simplify the problem by excluding Ar extracted from pyroxene at highest temperature. We therefore include only steps observed below the sharp transitions in the apparent Ca/K ratio observed at high temperatures (~950 °C; Fig. 1) for calculating diffusion coefficients and our diffusion modeling described below. Although pyroxene could be included in all modeling, these data have negligible influence on constraining each sample's low temperature history, and thus do not warrant the additional complexity.

To quantify the kinetics of Ar diffusion from glass and plagioclase involves construction of a multiple-phase (MP) diffusion model constrained by the ^{37}Ar and ^{39}Ar release fractions. And, to account for the possibility of a range of diffusion domain sizes in these whole-rock samples (i.e., a range in the dimensions of K-glass and plagioclase grains in each sample), we also incorporate multiple diffusion domains (Lovera et al., 1991; Cassata et al., 2010). In constructing a model, our objective is to incorporate sufficient complexity to quantify the bulk diffusive behavior of Ar in these samples while minimizing the total number of free parameters. We find that models comprising two glass domains and one plagioclase domain adequately predict the ^{37}Ar and ^{39}Ar release fractions and calculated values of D/a^2 for each isotope. Cassata and Renne (2013) observed non-linear Arrhenius arrays in plagioclase crystals with similar compositions to those in the mare basalts studied here, with upward curvature apparent at intermediate heating temperatures. It is not clear if the apparent linearity observed in the ^{37}Ar data reflects the confluence of downward curvature associated with a range in grain sizes and upward curvature associated with structural transitions in plagioclase (Cassata and Renne, 2013). This is a reasonable expectation, as a range in diffusion dimensions is expected based on the grain size variations observed by EPMA. Thus the plagioclase diffusion parameters may not be accurate. However, as will be discussed below, the shape of the age spectrum is defined almost entirely by diffusive loss from K-glass. Thus inaccuracies in the inferred diffusion parameters of plagioclase do not significantly affect modeled thermal histories. The MP-MDD model parameters (discussed below) are optimized to reproduce the ^{39}Ar and ^{37}Ar-based Arrhenius plots and the apparent Ca/K spectra obtained from glass and plagioclase.

To constrain the activation energy, E_a, for Ar diffusion in K-glass and plagioclase, linear regressions were applied to extractions that yielded reproducible D/a^2 values at a given temperature (Fig. 2). For K-glass and plagioclase, typically the first 4–6 or 10–12 extractions were used in the linear regressions to ^{39}Ar or ^{37}Ar data, respectively. Values of E_a (Table 1) are consistent with published studies of Ar diffusivity in plagioclase and glass (e.g., Turner, 1971; Hazelton et al., 2003; Cassata et al., 2009; Cassata and Renne, 2013). We assigned the fraction of ^{39}Ar$_K$ contained within K-glass (the rest was assigned to plagioclase) based on the cumulative fraction of ^{39}Ar released prior to the middle of the sharp increase in apparent Ca/K ratios that identifies the transition of Ar diffusion from primarily K-glass to plagioclase. Although we don't expect the range of extraction temperatures for each phase to necessarily be distinct based on studies of phase-specific diffusion kinetics (Hazelton et al., 2003; Cassata et al., 2009; Cassata and Renne, 2013), we expect the sequence of thermal extractions to progress from K-glass at lowest extraction temperatures to plagioclase at intermediate temperatures (with pyroxene at the highest temperatures, as discussed above). As noted above, two domains were assigned to K-glass and one to plagioclase. Additional domains would improve the goodness of fit between the observed and modeled Arrhenius arrays, but are not necessary.

The proportion of ^{39}Ar$_K$ allocated to K-glass was distributed amongst the two domains based on the cumulative fraction of ^{39}Ar released before and after the departure from linearity observed on an $\ln(r/r_o)$ plot (the difference between the natural logarithm of a given D/a^2 value and that expected from extrapolation of the low-temperature linear Arrhenius relationship; Fig. 2, Lovera et al., 1991). The fraction of ^{37}Ar$_{Ca}$ contained within each K-glass domain and the frequency factor (D_o/a^2) of each domain were free parameters to optimize the goodness of fit between the modeled and observed Arrhenius plots and Ca/K spectra. The accuracy of domain distribution parameter assigned using this approach can be assessed by comparison with the modal abundances and chemical compositions of plagioclase and K-glass (Table S2; e.g., Shea et al., 2012).

The MP-MDD model parameters quantified by this procedure are summarized in Table 1. Each MP-MDD model ultimately has 9 free parameters, although 4 of the 9 free parameters are objectively assigned (as discussed above). Our MP-MDD models indicate that K-glass is expected to lose a small fraction of Ar (<5% from the least retentive domain) during irradiation heating and extraction-line bake-out (average temperature of ~260 °C; Shuster and Farley, 2009). All models included this heating prior to the laboratory schedule to simulate diffusive loss during irradiation and extraction-line bake-out. Assuming that the Ar diffusion kinetics observed in the laboratory is adequately described by an optimized MP-MDD model, and that the kinetics can be extrapolated in both time and temperature, this information can be used to test various thermal conditions on the moon that would result in the spatial distribution of radiogenic ^{40}Ar (^{40}Ar*) or cosmogenic ^{38}Ar (^{38}Ar$_{cos}$), as

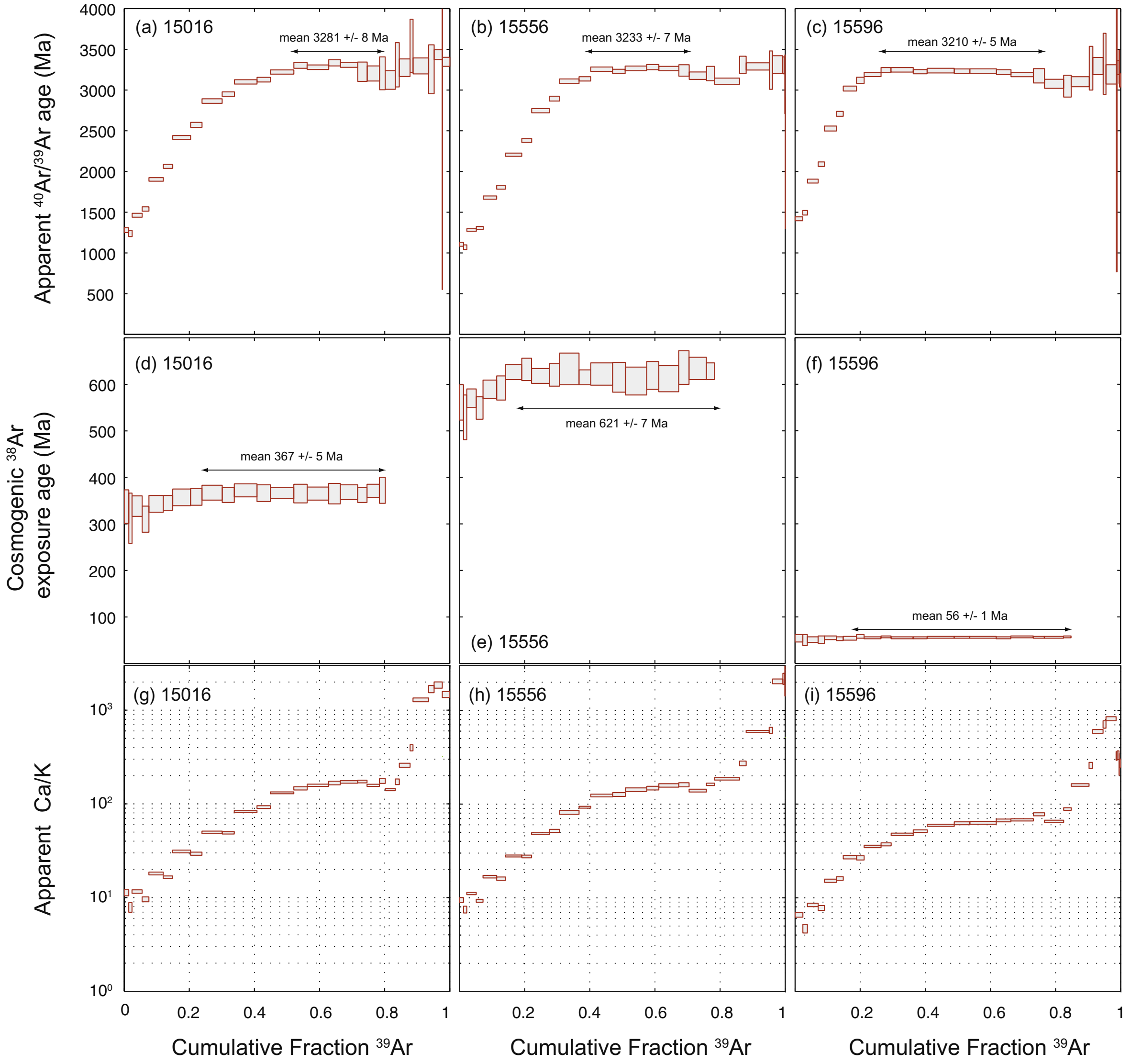

Fig. 1. Apparent ^{40}Ar/^{39}Ar age (a–c), ^{38}Ar/^{37}Ar (d–f) and Ca/K (g–i) spectra for three Apollo 15 samples. Each spectrum is plotted against the cumulative release fraction of ^{39}Ar. Dimensions of boxes indicate ±1 standard deviation (vertical) and the fraction of ^{39}Ar released (horizontal). Ca/K ratios were calculated from the $^{37}\text{Ar}_{\text{Ca}}/^{39}\text{Ar}_{\text{K}}$ ratio assuming that the relative production ratio for Ca to K is 1:1.96. Shifts in this apparent ratio help distinguish between dominant source phases of Ar during thermal extractions.

constrained by observed ^{40}Ar*/^{39}Ar and $^{38}\text{Ar}_{\text{cos}}/^{37}$Ar step-wise release spectra. Importantly, these calibrated models provide the temperature sensitivity of ^{40}Ar and ^{38}Ar retentivity that is specific to each analyzed sample.

2.5. Numerical methods

We developed a numerical model that predicts the ^{40}Ar/^{39}Ar and ^{38}Ar/^{37}Ar release spectra for input parameters that include the MP-MDD model specific to each sample and an arbitrary thermal model through geologic time. The model for ^{40}Ar and ^{38}Ar accumulation and diffusion through time uses a Crank–Nicholson finite-difference scheme for diffusion in a sphere as described by Ketcham (2005). A calculation for each domain within each phase predicts the abundance and spatial distribution of both isotopes in each. In these calculations, production of cosmogenic ^{38}Ar occurs at a constant rate that depends on the K, Ca, Fe and Ni concentrations within each domain solely since the apparent ^{38}Ar exposure age of each sample, whereas radiogenic ^{40}Ar is produced over all time since the apparent plateau age following exponential decay. To simulate ^{38}Ar and ^{40}Ar diffusion due to solar heating, we calculate daytime heating (over half of the lunar day) as an oscillatory square temperature wave. To simulate ^{40}Ar diffusion during impact heating, we calculate a square temperature pulse at a hypothetical timing of an impact.

The laboratory-degassing model that predicts ^{40}Ar/^{39}Ar and ^{38}Ar/^{37}Ar release spectra uses the same finite-difference method as the geologic model. The initial condition for the radial ^{40}Ar and ^{38}Ar distributions is taken from the end state of the geologic models, while the initial ^{39}Ar and

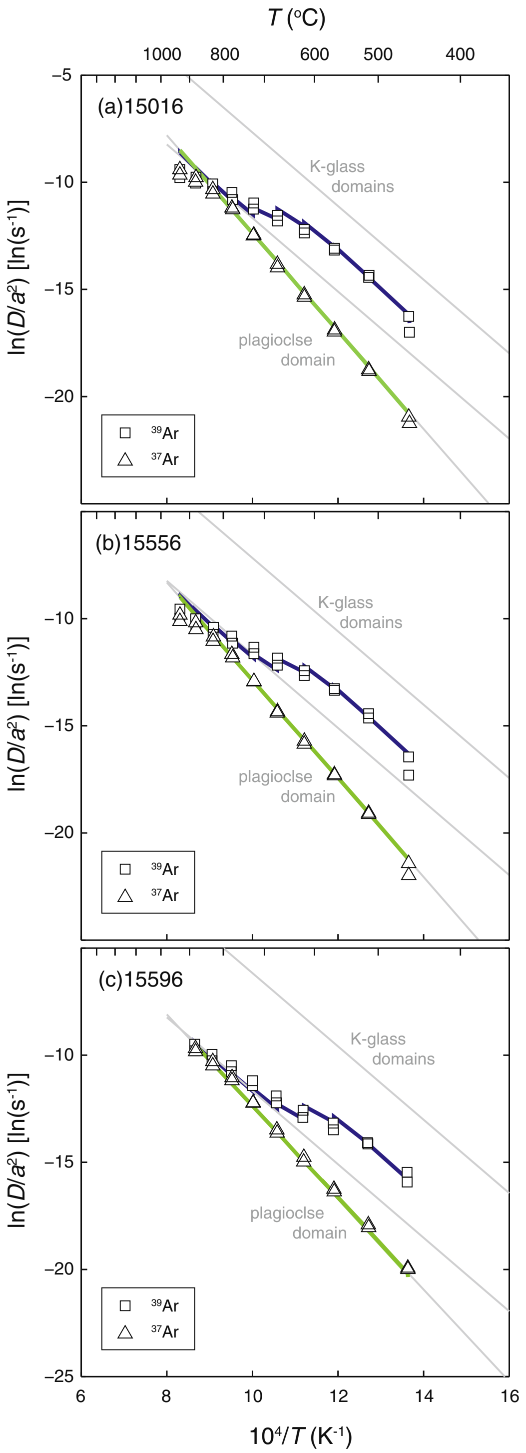

Fig. 2. ^{39}Ar and ^{37}Ar Arrhenius plots. Diffusivity as a function of temperature calculated (Fechtig and Kalbitzer, 1966) from ^{37}Ar and ^{39}Ar released during the first 21 heating steps; points are diffusion coefficients (D) divided by the square of the effective diffusive length-scale (a). T is the controlled temperature during the laboratory extraction. The blue and green curves represent the MP-MDD model fit to the data; grey lines are diffusion kinetics of the three model domains (see Table 1 for model parameters). (For interpretation of the references to color in this figure legend, the reader is referred to the web version of this article.)

^{37}Ar distributions are spatially uniform within each domain. To predict laboratory degassing, we use the MP-MDD model parameters, and the same heating schedule as used in the analyses. To predict whole-rock release spectra, the calculated releases of each isotope from each domain are summed and ratioed.

To quantify the goodness of fit between a particular model and the observed radioisotopic and exposure spectra, we calculate a reduced chi squared (χ_{ν}^2) misfit statistic (Bevington and Robinson, 1969). For a given model type (e.g., solar or impact heating), this statistic is calculated for a range of values of a single model parameter (e.g., the effective diffusion temperature or Dt/a^2). The minimum in the χ_{ν}^2 statistic identifies the best fitting model of a given model type.

3. RESULTS

3.1. ^{40}Ar/^{39}Ar and ^{38}Ar/^{37}Ar release spectra

Release spectra are shown in Fig. 1 as calculated ^{40}Ar/^{39}Ar step ages, cosmogenic ^{38}Ar exposure ages calculated for each step, and apparent Ca/K ratios plotted against the cumulative fraction of ^{39}Ar released. All three samples have similar ^{40}Ar/^{39}Ar age spectra, with low initial ages between 1000–1500 Ma, followed by a systematic increase in step ages over the subsequent ~25–50% of ^{39}Ar release to concordant ages that appear as plateaus. The apparent plateau ages are 3210 ± 5 Ma (15596), 3233 ± 7 Ma (15556), and 3281 ± 8 Ma (15016); uncertainties are 1 standard deviation, and include uncertainty in the decay constant and the age of the fluence monitor (Renne et al., 2011). Although reported here at higher precision, the ages of 15016 and 15556 agree with available chronologic constraints: Evensen et al. (1973) reported a Rb/Sr age of 3.29 ± 0.05 Ga and Kirsten et al. (1972) reported an ^{40}Ar/^{39}Ar plateau age of 3.28 ± 0.08 Ga for 15016 (recalculated using the decay constant of Steiger and Jäger (1977)); Kirsten et al. (1972) reported a K-Ar age of ~3.3 ± 0.1 Ga for 15556 (recalculated; Steiger and Jäger, 1977). We are not aware of any published chronologic constraints on 15596. Despite similarity in their ^{40}Ar/^{39}Ar plateau ages, the three samples have very different cosmogenic ^{38}Ar exposure ages estimated from the plateaus shown in Fig. 1d–f, which range from ~56 Ma (15596) to ~367 Ma (15016) to ~621 Ma (15556). While the ^{38}Ar/^{37}Ar ratios measured for 15556 and 15596 are relatively uniform, the ratios for 15016 show a sharp increase at 80% of ^{39}Ar release. This ^{39}Ar release fraction corresponds to a sharp increase in the apparent Ca/K ratios observed in all three samples. All three Ca/K spectra are similar, and consistent with Ar diffusion from three distinct phases with different E_a: one phase with relatively low Ca/K with low retentivity of Ar that is degassed over the first ~50% of ^{39}Ar release, a higher retentivity phase with intermediate Ca/K over the next ~30%, and a very high retentivity phase with high Ca/K over the final ~20%, although in detail, and at certain temperature intervals, Ar would have been released from multiple phases simultaneously.

3.2. ^{39}Ar and ^{37}Ar Arrhenius plots

Diffusion coefficients (D/a^2) calculated from the first 21 extractions of both ^{37}Ar and ^{39}Ar for all three samples are shown in Fig. 2. In each sample, nearly all of the values calculated for ^{37}Ar plot along a single, well-defined line, whereas the ^{39}Ar values are more complex. The coefficients calculated for ^{39}Ar are initially higher than ^{37}Ar by several orders of magnitude, yet the values for each isotope converge at high release fractions (>60%) at high temperature (>800 °C). Since ^{37}Ar is produced primarily from Ca, and since the K-glass contains a relatively small proportion of Ca in these samples, a regression through the ^{37}Ar data collected below 800 °C provides an estimate of the effective kinetics of Ar diffusion from plagioclase from a single domain size. As noted above, it is possible that the apparent linearity in plagioclase reflects a confluence of downward curvature associated with a range in grain sizes and upward curvature associated with structural transitions, and a second plagioclase model domain could predict the small departures from linearity at high temperatures. However, incorporating these complexities into the models would have negligible influence on Ar diffusivity calculated at low temperatures, so we do not include these in our analysis. Since both the K-glass and plagioclase contain K, the coefficients calculated for ^{39}Ar reflect diffusion from both phases. The high initial ^{39}Ar values of D/a^2 reflect the higher proportion of K relative to Ca in the K-rich glass, which has significantly higher diffusivity at low temperatures and dominates the ^{39}Ar release. Excluding the initial steps, which may be influenced by diffusive loss of ^{39}Ar from glass at elevated temperatures during neutron irradiation (Shuster and Farley, 2009; Cassata et al., 2010; Shuster et al., 2010) coefficients calculated from the initial 4–6 extractions plot along a linear array, which provides an estimate of the activation energy (E_a) for Ar diffusion in the K-glass. Over the subsequent extractions, the data depart from a linear array to eventually converge on the values calculated for ^{37}Ar.

3.3. MP-MDD model parameters

Following the methods described in Section 2.4.2, we minimized misfit between values calculated from the MP-MDD model and the observed release fractions of ^{37}Ar and ^{39}Ar (Fig. 2) by optimizing the free parameters in each model (Table 1). In all three samples, we find that an E_a of 143 kJ/mol predicts the ^{39}Ar observations; this activation energy is consistent with independent studies of Ar diffusivity in K-rich glass (e.g., Turner, 1971; Hazelton et al., 2003). Apportioning the initial 60–65% of the extracted ^{39}Ar between two K-glass diffusion domains of different size in roughly equal proportions predicts both the linearity in the initial steps, and the transition to lower values of D/a^2 observed between ~600 and 800 °C. The sizes of glass grains inferred from the diffusion data vary by factors of 15.6× in 15596, 9.5× in 15556, and 7.4× in 15016. These variations are consistent with the grain sizes observed by EPMA of a few microns up to 40 microns. Although using only 2 domains to model complex glass geometries and non-discrete grain sizes is a simplification, successful prediction of the ^{39}Ar Arrhenius plot indicates that the model adequately quantifies the bulk Ar diffusion kinetics in this aggregated material. To predict convergence of ^{37}Ar and ^{39}Ar values in the final 35–40% of extracted ^{39}Ar, we apportion these quantities of ^{39}Ar to a single plagioclase domain. In the three samples we find that an E_a of 178–190 kJ/mol predicts both the ^{37}Ar observations, and convergence in ^{39}Ar coefficients between K-glass and plagioclase. The model values for plagioclase E_a are well within the range of observed values for Ar diffusion kinetics in plagioclase (Cassata et al., 2009; Cassata and Renne, 2013).

3.4. Cosmogenic ^{38}Ar exposure age release spectra

Using the method described in Section 2.3, we convert the observed ^{38}Ar/^{37}Ar ratio of each step to an apparent cosmogenic ^{38}Ar exposure ages using the Ca/K ratio to estimate the ^{38}Ar production rate (Eq. (3)). When plotted against the cumulative release fraction of ^{37}Ar, this exposure age spectrum provides an observation that reflects the spatial distribution of cosmogenic ^{38}Ar within the diffusion domains of the samples (Fig. 3). For these spectra, we use the cumulative release of ^{37}Ar instead of ^{39}Ar as the ordinate axis since a greater proportion of the ^{38}Ar is produced from cosmic ray reactions on Ca than from K in these basaltic, plagioclase-rich rocks. As with ^{40}Ar/^{39}Ar age spectra, the initial steps can be interpreted as gas diffused initially from the outer edges of the least retentive diffusion domains (McDougall and Harrison, 1999). Therefore, as with the K–Ar system, quantitative models of production and diffusion of cosmogenic ^{38}Ar can be constructed and compared with the data. However, unlike radiogenic ^{40}Ar, the spatial distribution of ^{38}Ar would have resulted solely since the sample's exposure to cosmic rays within a few meters of the lunar surface (Hohenberg et al., 1978; Russ et al., 1972).

In each of the cosmogenic ^{38}Ar age spectra, we observe low apparent ages in the initial extractions, followed by a systematic increase to invariant ages (Fig. 3a–c). Unlike the ^{40}Ar/^{39}Ar age spectra, which have discordant ages observed over the initial ~30–55% of the ^{39}Ar released from K-glas and plagioclase (Fig. 3d–f), the discordant cosmogenic ^{38}Ar ages are only observed in the initial ~10% of the extracted ^{37}Ar from these two phases. And unlike the ^{40}Ar/^{39}Ar plateau ages, which differ by only ~2% between the three samples, the cosmogenic ^{38}Ar plateau ages vary by up to a factor of 10, from ~56 Ma (15596), to ~367 Ma (15016) to ~621 Ma (15556). When taken as lower bounds on each sample's surface exposure duration, these large difference in ^{38}Ar/^{37}Ar plateau ages indicate that the three samples experienced different events or processes that brought them to the lunar surface at very different points in time. The relatively young exposure age of 15596 is expected if the sampled boulder was derived from a greater depth of shielding at the edge of Hadley Rille (Meyer, 2005) and deposited atop bedrock that had more protracted surface exposure (e.g., as sampled by 15556). Our ~370 Ma exposure age for 15016 is similar to a ^{38}Ar exposure age reported by (Husain, 1974), and our ~620 Ma exposure age of 15556 is in good agreement with exposure duration constraints from ^{158}Gd/^{157}Gd ratios

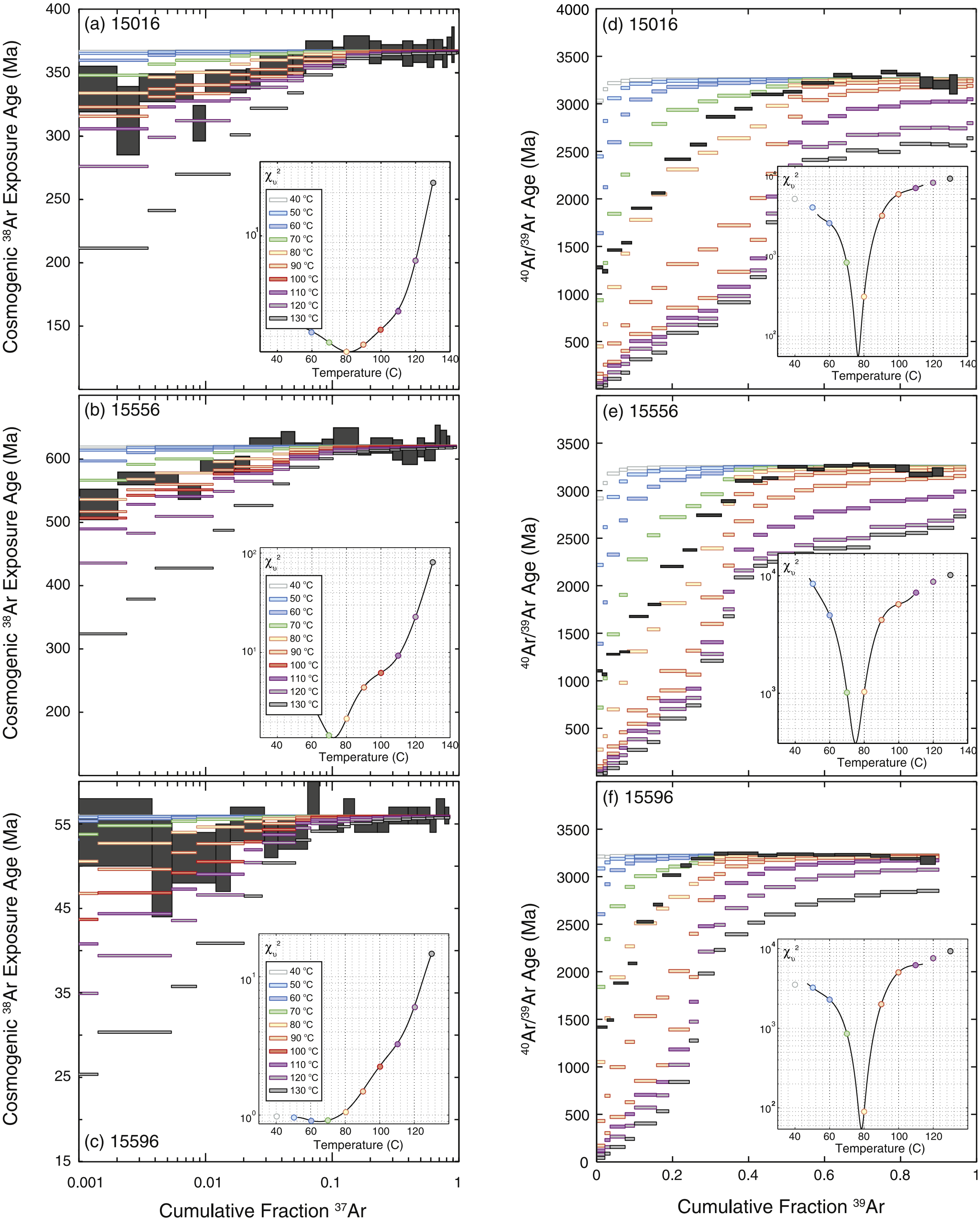

Fig. 3. Thermal constraints from production and diffusion of cosmogenic ^{38}Ar and radiogenic ^{40}Ar during exposure at the lunar surface. (a–c) Grey data are cosmogenic ^{38}Ar constraints expressed as apparent exposure ages ±1 standard deviation calculated from ^{38}Ar/^{37}Ar ratios as a function of the release fraction of ^{37}Ar and normalized to the first 21 heating steps (note log scale). Colored steps are predicted release spectra using the MP-MDD model parameters and for solar heating to temperatures ranging from 40 to 130 °C during the surface exposure of each sample. Insets show reduced chi squared (χ_ν^2) statistics of each fit, identifying ~65–81 °C as the best-fit effective diffusion temperatures (*EDT*s). (d–f) Diffusion of radiogenic ^{40}Ar due to solar heating. Grey data are the apparent ^{40}Ar/^{39}Ar ages plotted against the cumulative ^{39}Ar release fractions, normalized to the first 20 release steps. Colored steps are model release spectra for solar heating conditions, as in (a–c); inset identifies ~75–78 °C as the best-fit *EDT*s. Turner (1971) first proposed such diffusive loss of ^{40}Ar at the lunar surface. (For interpretation of the references to color in this figure legend, the reader is referred to the web version of this article.)

observed in the deep drill stem, also collected at station 9A (Russ et al., 1972). The very old ^{38}Ar exposure ages of 15016 and 15556 indicate that the bedrock at stations 3 and 9A each experienced protracted insolation and cosmic ray interactions.

3.5. Thermal constraints

Because the observed ^{40}Ar/^{39}Ar and cosmogenic ^{38}Ar exposure age spectra indicate open system, diffusive behavior (i.e., initially low ages that systematically increase to concordant ages at higher temperature extractions), we use these spectra and the calibrated MP-MDD models (Table 1, Fig. 2) to identify permissible thermal conditions of each sample at the lunar surface. Previous studies have found that both insolation (e.g., Turner, 1971; Shea et al., 2012) and impact-generated heat (e.g., Cassata et al., 2010; Shuster et al., 2010) can sufficiently elevate the temperatures of surface rocks to cause diffusive loss of both ^{40}Ar and ^{38}Ar. In this section, we use the Ar datasets of all three samples to quantitatively constrain the thermal conditions of each of these processes. Our modeling approach assumes that the observed diffusion kinetics and calibrated MP-MDD models (Fig. 2) quantify the kinetics of Ar diffusion in each sample over all time.

3.5.1. Solar heating models

In Fig. 3, we show results of production and diffusion models for solar heating of rocks at the lunar surface as both cosmogenic ^{38}Ar/^{37}Ar and ^{40}Ar/^{39}Ar age spectra. In each model, solar heating and diffusive loss of ^{38}Ar and ^{40}Ar occur solely since the apparent cosmogenic ^{38}Ar exposure age of each sample and for half of this duration due to oscillatory insolation; we calculate model spectra for *EDT*s ranging from 40–130 °C. For cosmogenic ^{38}Ar, production occurs solely (and continuously) during surface exposure. For radiogenic ^{40}Ar, production occurs since the apparent plateau age of each sample (Fig. 1), and is quantitatively retained (i.e., $D/a^2 = 0$) between that point in time and the cosmogenic ^{38}Ar exposure age.

For all three samples, the models predict cosmogenic ^{38}Ar and ^{40}Ar/^{39}Ar release spectra that are both in good agreement with the observed data. The best-fit value of *EDT* for each was identified by the minimum in a polynomial curve fit to χ^2_ν values for the range in T (Fig. 3, inset panels). The best-fit models of production and diffusion of cosmogenic ^{38}Ar correspond to *EDT*s that are statistically indistinguishable from one another, ranging from 65 $^{+15}/_{-338}$ °C (15596) to 81 $^{+20}/_{-18}$ °C (15016), despite exposure durations that vary by a factor of 10 between the three samples (Table 2; Fig. 1). Likewise, for ^{40}Ar, the best fitting *EDT*s of the three samples agree to within their estimated uncertainties, ranging from 75 ± 3 °C (15556) to 78 ± 2 °C (15596), and are in agreement with the *EDT*s for cosmogenic ^{38}Ar (Table 2) and the estimate of Turner (1971) (82 °C).

3.5.2. Impact heating models

In Fig. 4, we show as ^{40}Ar/^{39}Ar age spectra the results of production and diffusion models of impact heating for each

Table 2
Best fit heating models.

Sample	Apparent exposure age (Ma)	(+/−) (Ma)	Daytime heating models						Impact heating models					
			EDT [a] (°C)	(+/−)[b] (°C)	χ^2_υ	*EDT* [c] (°C)	(+/−)[b] (°C)	χ^2_υ	$\log_{10}(Dt/a^2)$[d]	(+/−)[b]	χ^2_υ	$\log_{10}(Dt/a^2)$[e]	(+/−)[b]	χ^2_υ
15016	367	5	81	$^{+20}/_{-18}$	1.6	77	2	74.0	−3.25	0.25	304.0	−3.03	0.25	237.1
15556	621	7	73	$^{+10}/_{-10}$	1.4	75	3	375.3	−3.02	0.20	479.5	−2.77	0.20	260.2
15596	56	1	65	$^{+15}/_{-\infty}$	0.9	78	2	57.6	−3.93	0.20	119.5	−3.70	0.20	139.6

[a] Best-fit effective diffusion temperature (*EDT*) for solar heating models fit to ^{38}Ar/^{37}Ar data.
[b] Standard deviations are estimated from values +1.2 units above minima in χ^2_υ.
[c] Best-fit *EDT* for solar heating models fit to ^{40}Ar/^{39}Ar data.
[d] Best fit Dt/a^2 value for impact heating at the apparent exposure age, fit to ^{40}Ar/^{39}Ar data.
[e] Best fit Dt/a^2 value for impact heating at 1000 Ma, fit to ^{40}Ar/^{39}Ar data.

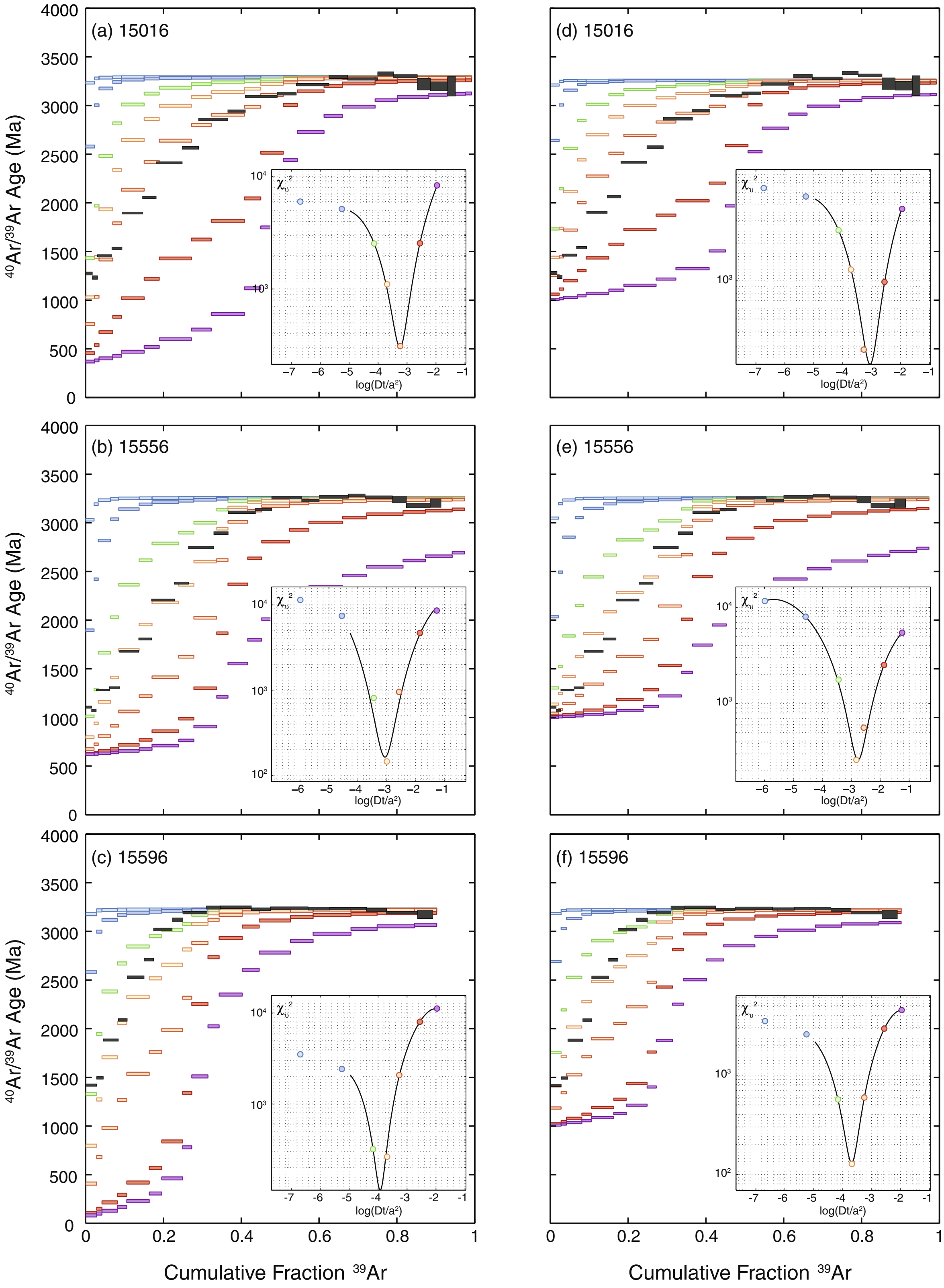

Fig. 4. Thermal constraints from diffusion of radiogenic ^{40}Ar during brief impact heating. Grey data are the apparent ^{40}Ar/^{39}Ar ages plotted against the cumulative ^{39}Ar release fractions, normalized to the first 21 heating steps. Colored steps are model release spectra for impact heating at the cosmogenic ^{38}Ar exposure age of each sample (a–c) and at 1000 Ma (d–f); insets identify the best-fit values of Dt/a^2 for these models. (For interpretation of the references to color in this figure legend, the reader is referred to the web version of this article.)

sample. Because the initial step ages of each restrict significant heating to have occurred at, or subsequent to, that point in time (Shuster et al., 2010), and to illustrate the influence of event timing, we predict the effects of impact heating of each sample at 1000 Ma (Fig. 4a–c) and at the sample's cosmogenic ^{38}Ar exposure age (Fig. 4d–f). In these calculations, radiogenic ^{40}Ar is quantitatively retained (i.e., $Dt/a^2 = 0$) within the diffusion domains of each sample, except for during a square pulse-heating event at either of these points in time. These two events may correspond to, and bound the timing of, impact events; for example, the latter models constrain the thermal conditions of events that may have exhumed each sample to the lunar surface.

We find that these impact-heating models are successful in predicting the observed ^{40}Ar/^{39}Ar spectra of all three samples. Best-fit models of this class are identified by a minimum in a polynomial curve fit to χ^2_ν for a range of Dt/a^2 values; here we compare Dt/a^2 values of the least retentive diffusion domain (i.e., the smallest glass domains that experienced most diffusive loss) in each MP-MDD model. The best-fit thermal models correspond to values of Dt/a^2 that, when extrapolated to other time temperature regimes based on the E_a of the glasses, constrain the durations and temperatures of the hypothetical reheating events. These extrapolations will result in different fractional losses for plagioclase domains because they have different E_a, but the differences are minor as they retain much of the gas. Values of $\log(Dt/a^2)$ for heating at the exposure age range from -3.9 ± 0.2 (15596) to -3.0 ± 0.2 (15556); values for heating at 1000 Ma range from -3.7 ± 0.2 (15596) to -2.8 ± 0.2 (15556) (Table 2). Under this set of assumptions, the best-fit values of Dt/a^2 place an upper bound on the duration-temperature pairs if all ^{40}Ar diffusion occurred at either of the two event times (Fig. 5). Alternatively, any reheating event that occurred between these points in time would plot between the curves shown in Fig. 5. However, because the initial step age of each sample is significantly younger than its plateau age, we find similar values of Dt/a^2 regardless of event timing. For all three samples, similar conditions during impact heating best predict the data. With the exception of the 1000 Ma model for sample 15556, the minimum χ^2_ν values for impact heating models are larger than those of daytime heating models fit to ^{40}Ar/^{39}Ar data (Table 2), indicating relatively poorer fits to the data.

4. DISCUSSION

4.1. Internal consistency between ^{38}Ar and ^{40}Ar diffusion models

Although our impact heating models adequately predicted the ^{40}Ar/^{39}Ar data (Fig. 4), the agreement between the best-fitting *EDT*s for cosmogenic ^{38}Ar and radiogenic ^{40}Ar (Fig. 3) indicates that both isotope systems likely experienced diffusive loss at the same thermal conditions solely due to solar heating during exposure at the lunar surface (Table 2). However, we can't exclude the possibility that multiple events and processes caused diffusive loss of ^{40}Ar from these samples. Because the effects of multiple heating conditions are additive, the solutions shown in Figs. 3 and 4 provide conservative upper bounds on the conditions of each model. For example, if impact heating occurred prior to surface exposure, the *EDT* for a subsequent solar heating model fit to ^{40}Ar/^{39}Ar data would be lower than that shown in Fig. 4 and Table 2.

When extrapolated to low temperatures, the best-fit Dt/a^2 values for ^{40}Ar/^{39}Ar models predicted by impact heating agree with the best-fit solar heating models for ^{38}Ar (Fig. 5), although the solar heating ^{40}Ar/^{39}Ar models provide better fit statistics (Table 2). In the solar heating models, diffusive loss of ^{38}Ar and ^{40}Ar occurs over very different proportions of each isotope's accumulation duration. Therefore, for a common *EDT* to predict the correct proportions of gas loss (i.e., >10 s of % diffusive loss of previously-accumulated ^{40}Ar, while simultaneously predicting only ~1–5% loss during cosmogenic ^{38}Ar production) provides an internal consistency test on that solution. For these reasons, we conclude that the thermal conditions expected for solar heating of the rocks provide the simplest explanation of each dataset. All *EDT* solutions are between ~65–81 °C, while error-weighted means of ^{38}Ar- and ^{40}Ar-derived *EDT*s range from 75–78 °C between the three samples. Despite differences in Ar diffusion kinetics (Table 1), and very different durations of surface exposure (Table 2), the internal consistency between all three datasets suggests that the samples experienced similar *EDT*s due to environmental conditions that were common between them.

4.2. Effective diffusion temperature versus mean annual temperature

Because Ar diffusivity is an exponential function of temperature, an *EDT* will not equal the mean annual temperature (*MAT*) of a rock that experiences temperature oscillations through time. In response to insolation, lunar surface temperatures vary by more than 250 °C over the course of a lunar day, while Ar diffusivity within a given diffusion domain can vary by ~60 orders of magnitude (Fig. 6; Huang, 2008; Bauch et al., 2009; Vasavada et al., 2012). Due to this nonlinearity, an *EDT* will be strongly biased toward maximum temperatures; relationships exist between an *EDT*, *MAT* and the amplitude of a simple periodic temperature oscillation (Turner, 1971; Tremblay et al., 2014). For example, for the lunar equatorial temperature cycle shown in Fig. 6 and the E_a of the K-glass in our MP-MDD models (143 kJ/mol), we expect a difference of ~155 °C between *EDT* and *MAT*, and only ~19 °C between *EDT* and the maximum temperature of surface exposed rock. Therefore, the full range of *EDT* solutions correspond to a range of *MAT* from −90 to −74 °C, and maximum daily temperatures between 84 and 110 °C. The weighted mean of the ^{38}Ar- and ^{40}Ar-based *EDTs* for all three samples (77.0 ± 1.3 °C) corresponds to a maximum temperature of ~96 °C, which is in excellent agreement direct temperature measurements of the lunar surface at the Apollo 15 landing site: the mean of maximum daytime temperatures observed over three calendar years is ~98 °C (Huang, 2008; data from archive PSPG-00093 of the US National Space Science Data Center). This indicates that,

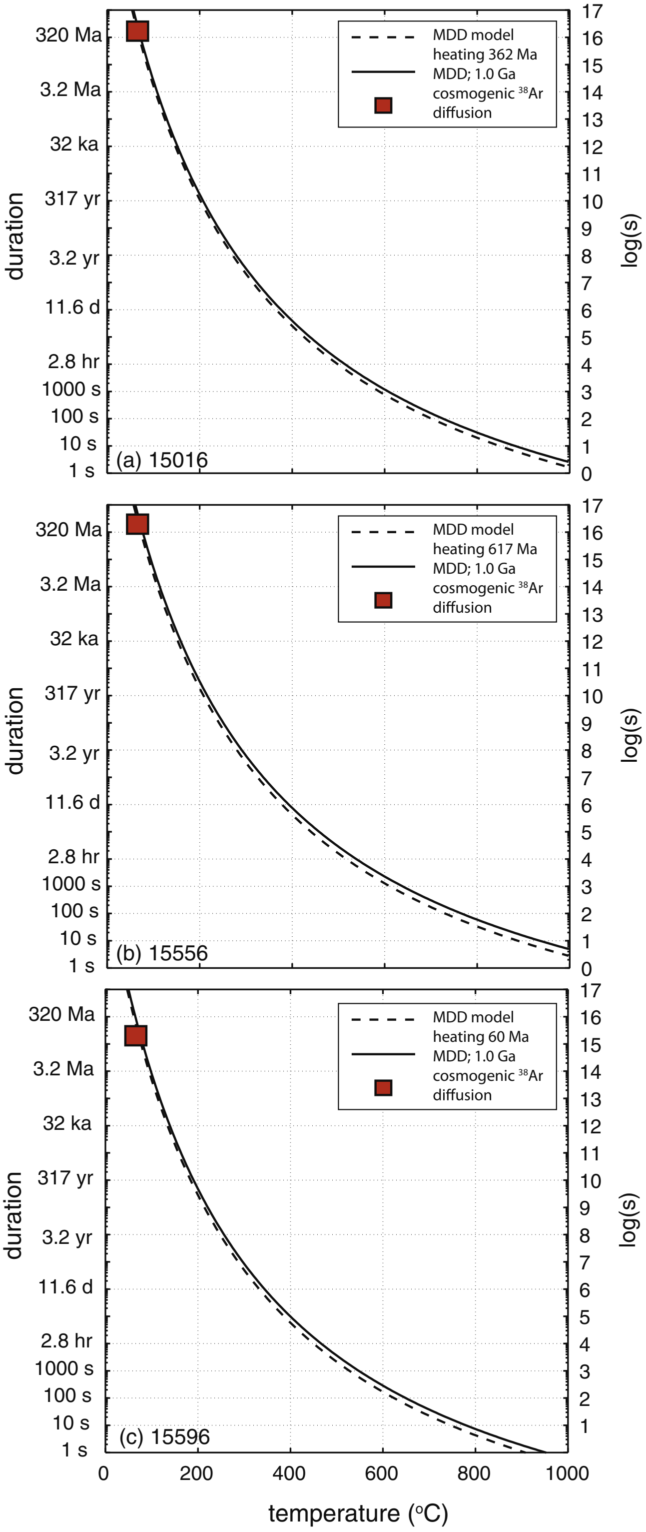

Fig. 5. Duration and temperature constraints on possible thermal excursions. Curves are elevated temperature conditions at the cosmogenic ^{38}Ar exposure age of each sample (dashed) and 1.0 Ga (solid) that would best predict the observed ^{40}Ar/^{39}Ar spectra shown in Fig. 4 using the MP-MDD models; squares are the best-fit solutions from production and diffusion of cosmogenic ^{38}Ar shown in Fig. 3.

over the last several hundred million years, the mean temperature at this site due to isolation could not have been significantly different from the modern.

Although the agreement in *EDT*s between the three samples and their agreement with direct temperature measurements indicate accuracy in the MDD model and its

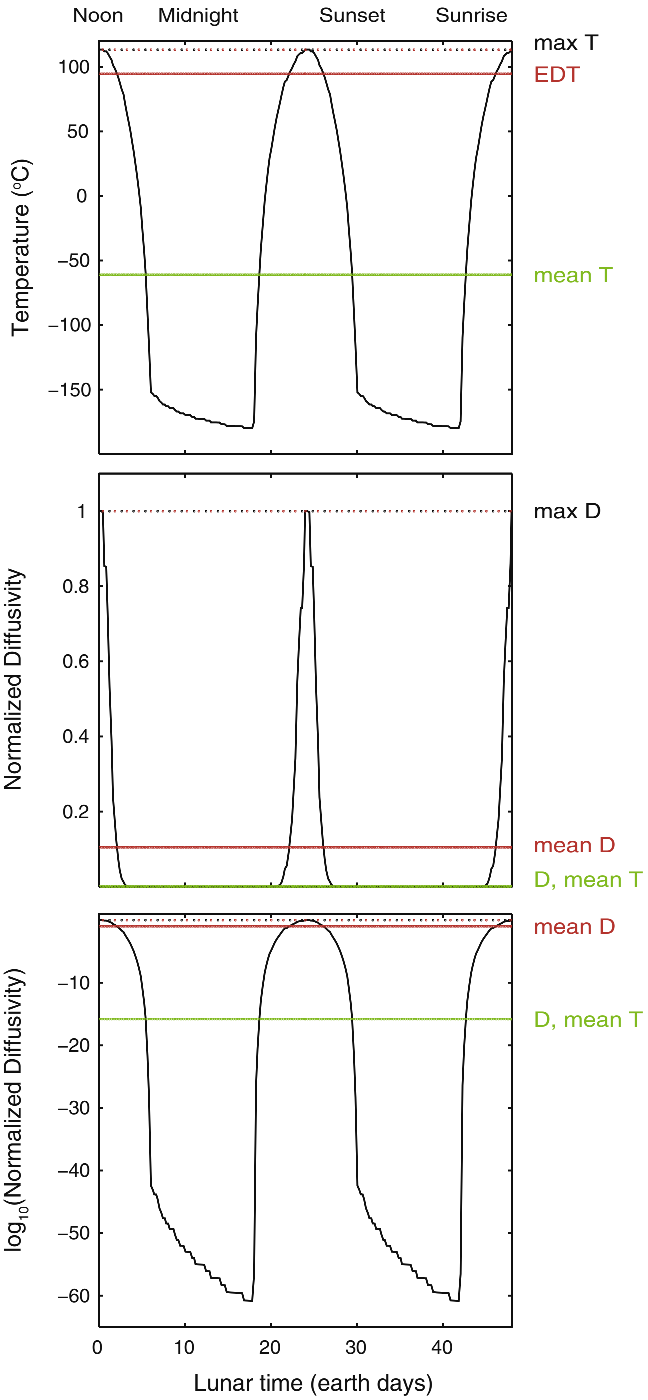

Fig. 6. Schematic illustration of the difference between effective diffusion temperature (*EDT*) and mean and maximum temperatures through the lunar daily insolation cycle. The *EDT* is calculated from the mean diffusivity *D* experienced over the temperature cycling shown in the upper panel (data are from the Diviner Lunar Radiometer Experiment; Vasavada et al., 2012), and will always be greater than or equal to the mean temperature since diffusivity is a nonlinear function of temperature. These data, from the lunar equator, indicate a difference of ~19 °C between the *EDT* and the maximum temperatures for $E_a = 143$ kJ/mol. The weighted mean *EDT*s of 75–78 °C observed for the three Apollo 15 samples are in good agreement with the modern temperatures observed at the Apollo 15 landing site.

governing parameters (Table 1), we do not formally account for two additional sources of uncertainty on our *EDT* solutions: uncertainties in the MP-MDD parameters and the ^{38}Ar production rate. The effects of uncertainty in (and potential inaccuracy of) the *MP-MDD* model parameters are difficult to evaluate, given that we are required to extrapolate Arrhenius relationships from laboratory conditions to lower temperatures expected at the lunar surface by more than 350 °C. For a diffusion domain with an assumed value of D_o, an underestimation (overestimation) of E_a would result in a lower (higher) apparent *EDT* for that model domain when extrapolated to lower temperatures. However, since D_o and E_a values determined by linear regression are correlated, the magnitude of this potential bias is limited. For example, in a very different type of application, Lovera et al. (1997) found internally-consistent thermal constraints when accounting for parameter uncertainty in MDD modeling of ^{40}Ar/^{39}Ar data from K-feldspar that experienced simple geologic cooling over ~30 Ma. Although not considered here, a more complete assessment of model uncertainty could be accomplished via reversible jump Markov Chain Monte Carlo type exploration of permissible MP-MDD model parameters (including the number of model domains; e.g., Green, 1995) and their influence on *EDT* solutions. Similarly, uncertainty in an assumed ^{38}Ar production rate will lead to uncertainty in both the exposure duration and the *EDT*s. For an observed ^{38}Ar/^{37}Ar release spectrum, an overestimation (underestimation) of the production rate would result in shorter (longer) apparent exposure duration, and higher (lower) apparent *EDT*. Although uncertainty in the production rate scales linearly with the exposure age uncertainty, the effect on *EDT* is relatively small. More significant, however, is our assumption that the samples resided solely at the lunar surface during ^{38}Ar production. If the samples instead resided at a depth above the e-folding depth of cosmogenic ^{38}Ar production, the shielding would cause both a lower ^{38}Ar production rate and a lower mean rock temperature due to thermal wave attenuation with depth arising from periodic insolation. For these reasons, our calculated exposure ages (Table 2) can be considered as lower bounds, although the differences between *EDT* and a sample's mean and maximum temperature would decrease with greater shielding (Tremblay et al., 2014).

4.3. Implications for paleomagnetic properties

Constraining the upper bounds on post-crystallization thermal conditions is important for the interpretation of natural remanent magnetization (NRM) observed in lunar samples and meteorites (e.g., Weiss et al., 2002; Garrick-Bethell et al., 2009; Fu et al., 2012). Since the primary thermoremanent magnetic properties of minerals can be modified by subsequent heating events, such as nearby volcanism or impact-generated heating at planetary surfaces, to establish when a NRM was acquired requires testing whether the sample could have exceeded its Curie temperature since crystallization. Therefore, to assign planetary surface field intensity estimates to points in time requires a quantitative understanding of each sample's thermal history since crystallization.

By conducting ^{40}Ar/^{39}Ar thermochronometry on the same samples characterized for NRM, our initial studies of lunar samples quantified upper bounds on hypothetical impact heating events, such as those shown in Section 3.5.2 (Garrick-Bethell et al., 2009; Shuster et al., 2010). For example, the curves shown in Fig. 5 provide bounds on both brief (seconds) shock-heating events, and more protracted conditions of diffusive heating in an ejecta blanket; either could reset a NRM if sufficiently hot. Therefore, if the temperature sensitivity of a sample's demagnetization is quantified (e.g., via thermal demagnetization experiments in the laboratory), the duration-temperatures curves shown in Fig. 5 can test the possibility of demagnetization since crystallization. If Ar thermochronometry excludes this possibility, then we can conclude that an observed NRM is primary and was established at or near the time of crystallization (e.g., as constrained by an ^{40}Ar/^{39}Ar plateau age).

Incorporating cosmogenic ^{38}Ar thermochronometry provides additional constraints for the interpretation of NRM in lunar samples (Shea et al., 2012; Suavet et al., 2013; Tikoo et al., 2014). All Apollo samples have experienced some amount of surface exposure and elevated temperatures due to insolation, although typically far below the Curie point of most materials. As shown in Fig. 3a–c, cosmogenic ^{38}Ar thermochronometry quantifies thermal conditions during surface exposure. By establishing whether some or all of the radiogenic ^{40}Ar diffusion could have occurred under these same conditions, the permissible impact heating conditions in Fig. 5 effectively shift to the left. In cases where all of the inferred ^{40}Ar diffusion is explained by the same thermal conditions inferred from ^{38}Ar, the intersection of both solutions (i.e., where the curves intersect the boxes in Fig. 5) provides a unique thermal solution for the sample. In such cases, as with the three samples studied here, the combined ^{40}Ar/^{39}Ar and ^{38}Ar/^{37}Ar data strongly exclude the possibility of significant loss of ^{40}Ar, hence likely exclude post-crystallization resetting of the samples' paleomagnetic properties.

4.4. Implications for ^{40}Ar/^{39}Ar and surface exposure dating on the moon and crater chronology

An important implication of our results is that radiogenic ^{40}Ar is not quantitatively retained in glass exposed at the lunar surface. As ^{40}Ar/^{39}Ar dating of impact melt breccias and glassy impact spherules provides the primary constraints on the absolute cratering chronology of the moon [e.g., Dalrymple and Ryder, 1996; see review by Stöffler et al. (2006)], inaccuracies associated with Ar loss at the lunar surface merit consideration. While incremental heating results are likely not problematic if reasonable plateau criteria are adopted, total fusion analyses and laser probe spot analyses (e.g., Müller et al., 1977; Eichhorn et al., 1978) may be systematically biased toward young ages. Samples from equatorial latitudes with appreciable exposure durations are particularly susceptible to diffusive ^{40}Ar loss. It is possible that much of the discordance observed on age spectra obtained from glassy lunar samples may simply reflect daytime heating at lunar surface temperatures (e.g., Turner, 1971; Gombosi et al., 2015).

Likewise, cosmogenic ^{38}Ar is not quantitatively retained in glass exposed at the lunar surface. As most ^{38}Ar exposure ages reported for lunar samples reflect total gas analyses (as opposed into incremental heating plateaus), literature results for samples containing glass may be systematically biased toward younger ages. It is likely that ^{21}Ne$_{cos}$ and ^{3}He$_{cos}$ exposure ages are also biased toward younger ages, as Ne and He diffusive more rapidly than Ar in comparable minerals (Baxter, 2010; Gourbet et al., 2012). However, the magnitude of such an effect is difficult to assess, as He and

Ne are not co-located with Ar in feldspars and glasses. For example, $^{21}Ne_{cos}$ is produced primarily from Mg hosted in olivine and pyroxene (Eugster and Michel, 1995), both of which are considerably more retentive of noble gases than feldspars and glasses (Shuster et al., 2004; Cassata et al., 2011; Gourbet et al., 2012; Cassata and Renne, 2013). Regardless, it seems probable that Xe- and Kr-based exposure ages are most accurate in glass-bearing samples with appreciable exposure durations given their lower diffusivity.

5. CONCLUSIONS

A combined analysis of sequentially degassed $^{38}Ar/^{37}Ar$ and $^{40}Ar/^{39}Ar$ release spectra measured on neutron-irradiated samples provides a method for quantifying time-integrated paleotemperatures of rocks exposure at the lunar surface. The simultaneous analysis of multiple isotope systems that experienced diffusive loss from phases with different temperature sensitivity provides significant leverage on permissible temperatures through time. Incorporating numerical models of cosmogenic ^{38}Ar production and diffusion with MP-MDD $^{40}Ar/^{39}Ar$ thermochronometry enables internal consistency tests that can distinguish between brief impact heating and protracted insolation at planetary surfaces and quantify the permissible thermal conditions of each process. In three samples from Apollo 15, we find that all datasets indicate open system behavior in both cosmogenic ^{38}Ar and radiogenic ^{40}Ar, and can be explained by diffusive Ar loss primarily from potassium-rich aluminosilicate glass due to solar heating of the rocks while they were exposed at the lunar surface. We calculate effective diffusion temperatures between 75 and 78 °C during exposure that correspond to rock maximum temperatures between 94 and 97 °C, which are in good agreement with surface temperatures directly observed at the Apollo 15 landing site. Diffusive loss of radiogenic ^{40}Ar from glass at these temperatures has important implications for the absolute calibration of the lunar crater chronology; failure to account this open system behavior would introduce a systematic bias to total gas $^{40}Ar/^{39}Ar$ ages and $^{38}Ar_{cos}$ exposure ages of lunar samples. Distinguishing between impact-generated and solar heating has important implications for the interpretation of paleomagnetic properties observed in planetary materials, by testing whether samples were above their curie points since crystallization. Further, quantifying the thermal conditions of surface-exposed rocks is important for assessing environmental conditions necessary for biota and liquid water. In principle, this method could be applied to rocks returned from the surface of Mars, or with appropriate instrumentation at the Martian surface (Farley et al., 2014), to quantify time-integrated thermal conditions of regolith and bedrock during surface exposure.

ACKNOWLEDGMENTS

We thank the Apollo 15 team, the Johnson Space Center staff and the Curation and Analysis Planning Team for Extraterrestrial Samples for allocating the samples, B. Weiss and S. Tikoo for helpful discussions, and T. Becker and N. Fylstra for laboratory support and Sean Mulcahy for assistance with EPMA. This manuscript benefited from reviews provided by two anonymous reviewers, G. Turner, and Associate Editor G. Herzog. Funding was provided by the following sources: NASA Lunar Advanced Science and Exploration Research program (grant # NNX08AY96G; subaward to DLS), and the Ann and Gordon Getty Foundation.

APPENDIX A. SUPPLEMENTARY DATA

Complete datasets of Ar isotopic analyses of stepwise degassing experiments. Supplementary data associated with this article can be found, in the online version, at http://dx.doi.org/10.1016/j.gca.2015.01.037.

REFERENCES

Bauch K., Hiesinger H. and Helbert J. (2009) Estimation of lunar surface temperatures: a numerical model. *40th Lunar Planet. Sci. Conf. Proc.*, p. 1789.

Baxter E. F. (2010) Diffusion of noble gases in minerals. *Rev. Mineral. Geochem.* **72**, 509–557.

Bevington P. R. and Robinson D. K. (1969) *Data Reduction and Error Analysis for the Physical Sciences*. McGraw-Hill, New York.

Brown G., Emeleus C., Holland J., Peckett A. and Phillips R. (1972) Mineral-chemical variations in Apollo 14 and Apollo 15 basalts and granitic fractions. *Lunar Planet. Sci. Conf. Proc.*, p. 141.

Butler P. (1971) Lunar sample catalog, Apollo 15. In (ed. M. Curators' Office).

Cassata W. S. and Renne P. R. (2013) Systematic variations of argon diffusion in feldspars and implications for noble gas thermochronometry. *Geochim. Cosmochim. Acta* **112**, 251–287.

Cassata W. S., Renne P. R. and Shuster D. L. (2009) Argon diffusion in plagioclase and implications for thermochronometry: a case study from the Bushveld Complex, South Africa. *Geochim. Cosmochim. Acta* **73**, 6600–6612.

Cassata W. S., Renne P. R. and Shuster D. L. (2011) Argon diffusion in pyroxenes: implications for thermochronometry and mantle degassing. *Earth Planet. Sci. Lett.* **304**(3), 407–416.

Cassata W. S., Shuster D. L., Renne P. R. and Weiss B. P. (2010) Evidence for shock heating and constraints on Martian surface temperatures revealed by $^{40}Ar/^{39}Ar$ thermochronometry of Martian meteorites. *Geochim. Cosmochim. Acta* **74**, 6900–6920.

Dalrymple G. B. and Ryder G. (1996) Argon-40/argon-39 age spectra of Apollo 17 highlands breccia samples by laser step heating and the age of the Serenitatis basin. *J. Geophys. Res.: Planets (1991–2012)* **101**, 26069–26084.

Eichhorn G., Schaeffer O., James O. and Müller H. (1978) Laser $^{39}Ar–^{40}Ar$ dating of two clasts from consortium breccia 73215. *Lunar Planet. Sci. Conf. Proc.*, pp. 855–876.

Eugster O. and Michel T. (1995) Common asteroid break-up events of eucrites, diogenites, and howardites and cosmic-ray production rates for noble gases in achondrites. *Geochim. Cosmochim. Acta* **59**, 177–199.

Evensen N., Murthy V. R., Coscio, Jr., M. (1973) Rb-Sr ages of some mare basalts and the isotopic and trace element systematics in lunar fines. *Lunar Planet. Sci. Conf. Proc.*, p. 1707.

Farley K., Malespin C., Mahaffy P., Grotzinger J., Vasconcelos P., Milliken R., Malin M., Edgett K., Pavlov A. and Hurowitz J. (2014) In situ radiometric and exposure age dating of the Martian surface. *Science* **343**, 1247166.

Fechtig H. and Kalbitzer S. (1966) The diffusion of argon in potassium bearing solids. In *Potassium-Argon Dating* (eds. O. A. Schaeffer and J. Zahringer). Springer, Heidelberg, pp. 68–106.

Fu R. R., Weiss B. P., Shuster D. L., Gattacceca J., Grove T. L., Suavet C., Lima E. A., Li L. and Kuan A. T. (2012) An ancient core dynamo in asteroid Vesta. *Science* **338**, 238–241.

Garrick-Bethell I., Weiss B. P., Shuster D. L. and Buz J. (2009) Early lunar magnetism. *Science* **323**, 356–359.

Gault D., Hörz F., Brownlee D. and Hartung J. (1974) Mixing of the lunar regolith. *Lunar Planet. Sci. Conf. Proc.*, pp. 2365–2386.

Gombosi D. J., Baldwin S. L., Watson E. B., Swindle T. D., Delano J. W. and Roberge W. G. (2015) Argon diffusion in Apollo 16 impact glass spherules: Implications for ^{40}Ar/^{39}Ar dating of lunar impact events. *Geochim. Cosmochim. Acta* **148**, 251–268.

Gourbet L., Shuster D. L., Balco G., Cassata W. S., Renne P. R. and Rood D. (2012) Neon diffusion kinetics in olivine, pyroxene and feldspar: retentivity of cosmogenic and nucleogenic neon. *Geochim. Cosmochim. Acta* **86**, 21–36.

Green P. J. (1995) Reversible jump Markov chain Monte Carlo computation and Bayesian model determination. *Biometrika* **82**, 711–732.

Grove T. L. and Walker D. (1977) Cooling histories of Apollo 15 quartz-normative basalts. *Lunar Planet. Sci. Conf. Proc.*, pp. 1501–1520.

Hazelton G. B., Axen G. and Lovera O. (2003) Argon retention properties of silicate glasses and implications for ^{40}Ar/^{39}Ar age and noble gas diffusion studies. *Contrib. Miner. Petrol.* **145**, 1–14.

Hohenberg C., Podosek F., Shirck J., Marti K. and Reedy R. (1978) Comparisons between observed and predicted cosmogenic noble gases in lunar samples. *Lunar Planet. Sci. Conf. Proc.*, 2311–2344.

Huang S. (2008) Surface temperatures at the nearside of the Moon as a record of the radiation budget of Earth's climate system. *Adv. Space Res.* **41**, 1853–1860.

Husain L. (1974) ^{40}Ar-^{39}Ar chronology and cosmic ray exposure ages of the Apollo 15 samples. *J. Geophys. Res.* **79**, 2588–2606.

Jourdan F. and Renne P. (2009) Neutron-induced ^{37}Ar recoil ejection in Ca-rich minerals and implications for ^{40}Ar/^{39}Ar dating. *Geochim. Cosmochim. Acta Suppl.* **73**, 606.

Jourdan F., Matzel J. P. and Renne P. R. (2007) ^{39}Ar and ^{37}Ar recoil loss during neutron irradiation of sanidine and plagioclase. *Geochim. Cosmochim. Acta* **71**, 2791–2808.

Ketcham R. A. (2005) Forward and inverse modeling of low-temperature thermochronometry data. *Rev. Mineral. Geochem.* **58**, 275–314.

Kirsten T., Deubner J., Horn P., Kaneoka I., Kiko J., Schaeffer O. and Thio S. (1972) The rare gas record of Apollo 14 and 15 samples. *Lunar Planet. Sci. Conf. Proc.*, 1865–1889.

Korochantseva E. V., Trieloff M., Lorenz C. A., Buykin A. I., Ivanova M. A., Schwarz W. H., Hopp J. and Jessberger E. K. (2007) L-chondrite asteroid breakup tied to Ordovician meteorite shower by multiple isochron ^{40}Ar–^{39}Ar dating. *Meteorit. Planet. Sci.* **42**, 113–130.

Levine J., Renne P. R. and Muller R. A. (2007) Solar and cosmogenic argon in dated lunar impact spherules. *Geochim. Cosmochim. Acta* **71**, 1624–1635.

Lovera O. M., Richter F. M. and Harrison T. M. (1991) Diffusion domains determined by ^{39}Ar released during step heating. *J. Geophys. Res.: Solid Earth (1978–2012)* **96**, 2057–2069.

Lovera O. M., Grove M., Mark Harrison T. and Mahon K. (1997) Systematic analysis of K-feldspar ^{40}Ar^{39}Ar step heating results: I. Significance of activation energy determinations. *Geochim. Cosmochim. Acta* **61**, 3171–3192.

McDougall I. and Harrison T. M. (1999) *Geochronology and Thermochronology by the* ^{40}*Ar*/^{39}*Ar Method*. Oxford University Press.

McGee P., Warner J. and Simonds C. (1977) Introduction to the Apollo collections. Part 1: lunar igneous rocks. *NASA STI/Recon. Tech. Rep. N* **77**, 22034.

Meyer C. (2005) Lunar sample compendium. *NASA STI/Recon. Tech. Rep. N* **6**, 11039.

Müller H., Schaeffer O., Plieninger T. and James O. (1977) Laser probe/Ar-39/–/Ar-40/dating of materials from consortium breccia 73215. *Lunar Planet. Sci. Conf. Proc.*, 2551–2565.

Papike J., Hodges F., Bence A., Cameron M. and Rhodes J. (1976) Mare basalts: crystal chemistry, mineralogy, and petrology. *Rev. Geophys.* **14**, 475–540.

Renne P. R., Knight K. B., Nomade S., Leung K.-N. and Lou T.-P. (2005) Application of deuteron–deuteron (D–D) fusion neutrons to ^{40}Ar/^{39}Ar geochronology. *Appl. Radiat. Isot.* **62**, 25–32.

Renne P. R., Balco G., Ludwig K. R., Mundil R. and Min K. (2011) Response to the comment by WH Schwarz et al. on "Joint determination of ^{40}K decay constants and ^{40}Ar*/^{40}K for the Fish Canyon sanidine standard, and improved accuracy for ^{40}Ar/^{39}Ar geochronology" by PR Renne et al. (2010). *Geochim. Cosmochim. Acta* **75**, 5097.

Rhodes J. and Hubbard N. (1973) Chemistry, classification, and petrogenesis of Apollo 15 mare basalts. *Lunar Planet. Sci. Conf. Proc.*, p. 1127.

Richter F. M., Lovera O. M., Mark Harrison T. and Copeland P. (1991) Tibetan tectonics from ^{40}Ar/^{39}Ar analysis of a single K-feldspar sample. *Earth Planet. Sci. Lett.* **105**, 266–278.

Russ, III, P., Burnett D. and Wasserburg G. (1972) Lunar neutron stratigraphy. *Earth Planet. Sci. Lett.* **15**, 172–186.

Ryder G. and Spudis P. (1987) Chemical composition and origin of Apollo 15 impact melts. *J. Geophys. Res.: Solid Earth (1978-2012)* **9**, E432–E446.

Shea E. K., Weiss B. P., Cassata W. S., Shuster D. L., Tikoo S. M., Gattacceca J., Grove T. L. and Fuller M. D. (2012) A long-lived lunar core dynamo. *Science* **335**, 453–456.

Shuster D. L. and Farley K. A. (2009) The influence of artificial radiation damage and thermal annealing on helium diffusion kinetics in apatite. *Geochim. Cosmochim. Acta* **73**, 183–196.

Shuster D. L., Farley K. A., Sisterson J. M. and Burnett D. S. (2004) Quantifying the diffusion kinetics and spatial distributions of radiogenic ^{4}He in minerals containing proton-induced ^{3}He. *Earth Planet. Sci. Lett.* **217**, 19–32.

Shuster D. L., Balco G., Cassata W. S., Fernandes V. A., Garrick-Bethell I. and Weiss B. P. (2010) A record of impacts preserved in the lunar regolith. *Earth Planet. Sci. Lett.* **290**, 155–165.

Steiger R. H. and Jäger E. (1977) Subcommission on geochronology: convention on the use of decay constants in geo-and cosmochronology. *Earth Planet. Sci. Lett.* **36**, 359–362.

Stöffler D., Ryder G., Ivanov B. A., Artemieva N. A., Cintala M. J. and Grieve R. A. (2006) Cratering history and lunar chronology. *Rev. Mineral. Geochem.* **60**, 519–596.

Suavet C., Weiss B. P., Cassata W. S., Shuster D. L., Gattacceca J., Chan L., Garrick-Bethell I., Head J. W., Grove T. L. and Fuller M. D. (2013) Persistence and origin of the lunar core dynamo. *Proc. Natl. Acad. Sci.* **110**, 8453–8458.

Tikoo S. M., Weiss B. P., Buz J., Lima E. A., Shea E. K., Melo G. and Grove T. L. (2012) Magnetic fidelity of lunar samples and implications for an ancient core dynamo. *Earth Planet. Sci. Lett.* **337**, 93–103.

Tikoo S. M., Weiss B. P., Cassata W. S., Shuser D. L., Gattacceca J., Lima E. A., Suavet C., Nimmo F. and Fuller M. D. (2014) Decline of the lunar core dynamo. *Earth Planet. Sci. Lett.*. http://dx.doi.org/10.1016/j.epsl.2014.07.010.

Tremblay M. M., Shuster D. L. and Balco G. (2014) Cosmogenic noble gas paleothermometry. *Earth Planet. Sci. Lett.* **400**, 195–205.

Turner G. (1971) ^{40}Ar-^{39}Ar ages from the lunar maria. *Earth Planet. Sci. Lett.* **11**, 169–191.

Turner G. and Cadogan P. (1974) Possible effects of ^{39}Ar recoil in ^{40}Ar–^{39}Ar dating. *Lunar Planet. Sci. Conf. Proc.*, 1601–1615.

Turner G., Huneke J., Podosek F. and Wasserburg G. (1971) ^{40}Ar-^{39}Ar ages and cosmic ray exposure ages of Apollo 14 samples. *Earth Planet. Sci. Lett.* **12**, 19–35.

Turner G., Knott S., Ash R. and Gilmour J. (1997) Ar–Ar chronology of the Martian meteorite ALH84001: evidence for the timing of the early bombardment of Mars. *Geochim. Cosmochim. Acta* **61**, 3835–3850.

Vasavada A. R., Bandfield J. L., Greenhagen B. T., Hayne P. O., Siegler M. A., Williams J. P. and Paige D. A. (2012) Lunar equatorial surface temperatures and regolith properties from the Diviner Lunar Radiometer Experiment. *J. Geophys. Res.: Planets* **1991–2012**, 117.

Villa I. M. (1997) Direct determination of ^{39}Ar recoil distance. *Geochim. Cosmochim. Acta* **61**, 689–691.

Weiss B. P., Vali H., Baudenbacher F. J., Kirschvink J. L., Stewart S. T. and Shuster D. L. (2002) Records of an ancient Martian magnetic field in ALH84001. *Earth Planet. Sci. Lett.* **201**, 449–463.

Wieler R. (2002) Noble gases in the solar system. *Rev. Mineral. Geochem.* **47**, 21–70.

Associate editor: Gregory F. Herzog